J. Marine Sci. Appl. (2014) 13: 158-166
DOI: 10.1007/s11804-014-1248-8

Numerical Study of Viscous Wave-Making Resistance of Ship Navigation in Still Water

Ruosi Zha, Haixuan Ye, Zhirong Shen and Decheng Wan*

State Key Laboratory of Ocean Engineering, School of Naval Architecture, Ocean and Civil Engineering, Shanghai Jiao Tong University, Shanghai 200240, China

Abstract: The prediction of a ship's resistance especially the viscous wave-making resistance is an important issue in CFD applications. In this paper, the resistances of six ships from hull 1 to hull 6 with different hull forms advancing in still water are numerically studied using the solver naoe-FOAM-SJTU, which was developed based on the open source code package OpenFOAM. Different components of the resistances are computed and compared while considering two speed conditions (12 kn and 16 kn). The resistance of hull 3 is the smallest while that of hull 5 is the largest at the same speed. The results show hull 3 is a good reference for the design of similar ships, which can provide some valuable guidelines for hull form optimization.
Keywords: ship navigation**;** CFD**;** wave-making resistance; viscous flow; hull; naoe-FOAM-SJTU solver; OpenFOAM

Article ID: 1671-9433(2014)02-0158-09

1 Introduction

It is naturally important for a ship to improve the energy conservation and economical efficiency by drag reduction. An accurate computation of a ship's resistances during the preliminary design phase of a ship building project does make sense. Large numbers of related methods have been developed in previous studies. Dawson (1977) studied a practical computer method for solving ship wave problems using the inviscid method. Bal (2008) investigated the wave pattern and wave resistance of the surface piercing bodies by use of a boundary element method. Numerical simulations based on CFD (computational fluid dynamics) are a powerful tool for the prediction of ship resistances and optimization of hydrodynamic performances. Especially with the advanced computer hardware and numerical methods, the efficiency and reliability of the CFD method have been greatly improved. Due to taking the fluid viscosity effects into account, a more realistic flow field and a better result to solve nonlinear problems can be obtained.

As an open source code package based on C++ libraries, OpenFOAM (Jasak *et al*., 2007) has a high degree of flexibility and expansibility to solve hydrodynamic problems. The solver naoe-FOAM-SJTU (Shen *et al.*, 2012) applied in this paper is developed depending on the data structures and basic solvers of OpenFOAM. In brief, this solver adopts the incompressible RANS equations as governing equations and the volume of fluid (VOF) method (Shen and Wan, 2013) to simulate the free surface of the two-phase flow. The finite volume method (FVM) (Hino *et al*., 1993) is used to discretize equations for arbitrary polyhedral grids. The pressure-velocity coupling equations are solved by use of the pressure-implicit with splitting of operations (PISO) algorithm (Barton, 1998). The wave generation and damping module (Cha and Wan, 2011), six-degree-of-freedom motion module (Weymouth *et al*., 2005) and coupled dynamic deformation mesh module were also developed to form a numerical tank system. The resistance is calculated by integrating the pressure force in X direction of each control volume along the wetted surface directly.

Much progress has been made with the unsteady Reynolds-Average navier stokes (URANS) method for viscosity simulations. According to the studies done in the past few years, the reliability and efficiency of naoe-FOAM-SJTU were improved and validated. Shen *et al*. (2011) simulated the viscous flow around the hulls of the KVLCC2, KCS, and DTMB5415 and compared the results of the measurements using naoe-FOAM-SJTU. Cao and Wan (2012) studied the extreme wave effects on cylindrical offshore structures by use of the naoe-FOAM-SJTU. Ye *et al*. (2012) studied the added resistance in regular head waves and validated the ability of naoe-FOAM-SJTU to solve the strong nonlinear problems.

In this paper, the still water resistance and the viscosity field of six research ships in full scale are studied by use of the naoe-FOAM-SJTU. The aim of this paper is to study the resistance components of special hull geometries in calm water and the influence of different Froude numbers, and to study the effects of different hull features and provide references for ship design with the aspect of hydrodynamic performance. The essential mathematical and numerical

Received date: 2014-01-05.
Accepted date: 2014-03-31.
Foundation item: Supported by the National Natural Science Foundation of China (Grant Nos.11072154, 51379125), the National Key Basic Research Development Plan (973 Plan) Project of China (Grant No.2013CB036103), the High Technology of Marine Research Project of the Ministry of Industry and Information Technology of China and the Program for Professor of Special Appointment (Eastern Scholar) at Shanghai Institutions of Higher Learning (Grant No. 2013022).
***Corresponding author Email:** dcwan@sjtu.edu.cn.

methods are explained in section 2. To validate the correctness of the programs and mesh systems, a benchmark computation on the KCS container ship is studied in section 3. The research ship models and meshes are shown in section 4. In section 5, analyses of the numerical results and post-processing results are presented.

2 Mathematical and numerical methods

2.1 Governing equations

The incompressible RANS equations are adopted as the governing equations. The SST k - ω turbulence model is applied to the present work. The equations of continuity and momentum can be written as:

$$\nabla \cdot U = 0 \tag{1}$$

$$\frac{\partial \rho U}{\partial t} + \nabla \cdot [\rho (U - U_g) U] = -\nabla p_d - g \cdot x \nabla \rho + \nabla \cdot (\mu_{\text{eff}} \nabla U) + (\nabla U) \cdot \nabla \mu_{\text{eff}} + f_\sigma + f_s \tag{2}$$

where U stands for the velocity field while U_g stands for the velocity of the mesh points. p_d is the dynamic pressure, obtained by subtracting the hydrostatic component from the total pressure. ρ is the mixture density of water and air. g represents the acceleration vector of gravity. μ_{eff} represents the effective dynamic viscosity coefficient, equaling to $\rho(\nu+\nu_t)$, where ν is the kinematic viscosity coefficient and ν_t is the eddy viscosity coefficient. f_σ is a surface tension term while f_s is the source term for the sponge layer to absorb the generated wave.

2.2 VOF method

The solver naoe-FOAM-SJTU adopts a VOF (volume of fluid) method with the artificial bounded compression technique for capturing the free surface. The VOF transport equation is formulated as:

$$\frac{\partial \alpha}{\partial t} + \nabla \cdot [(U - U_g)\alpha] + \nabla \cdot [U_r (1 - \alpha)\alpha] = 0 \tag{3}$$

where α is equivalent to the relative proportion of the two phase fluids. The value of α is:

$$\begin{cases} \alpha = 0 & \text{air} \\ \alpha = 1 & \text{water} \\ 0 < \alpha < 1 & \text{interface} \end{cases} \tag{4}$$

The surface tension term in Eq. (2) is defined as:

$$f_\sigma = \sigma \kappa \nabla \alpha \tag{5}$$

where σ is the surface tension, which is set as 0.07 kg/s^2 in the present work; κ is the curvature of the surface interface, defined as:

$$\kappa = -\nabla \cdot n = -\frac{\Sigma_f S_f \cdot n_f}{V_i} \tag{6}$$

in which V_i is the volume of the cell; the subscript f means that the value is computed at the cell face; $\sum_f S_f$ represents the sum magnitude of the face area where S_f is the normal vector of the cell face; n_f is the unit normal vector on the interface, written as Eq. (7), where δ is the stabilization factor.

$$n_f = \frac{(\nabla \alpha)_f}{|(\nabla \alpha)_f + \delta|} \tag{7}$$

Moreover, the first two terms on the left hand side of Eq. (3) stand for the traditional volume of the fluid transport equations and the other one represents the artificial compression term. The term $(1-\alpha)\alpha$ makes the compression term take effect only on the interface without affecting the numerical computation out of the transition layer. U_r is the velocity field for compressing the interface. The velocity field can be computed at the cell faces by the maximum velocity magnitude at the interface region, defined as:

$$U_{r,f} = n_f \min\left\{ C_\alpha \frac{|\phi|}{|S_f|}, \max\left(\frac{|\phi|}{|S_f|} \right) \right\} \tag{8}$$

where ϕ is the face volume flux, including the flux of the grid velocities from the PISO algorithm; C_α is a compression coefficient indicating the degree of compression.

2.3 Discretization of equations

The finite volume method (FVM) (Hino *et al*., 1993) is used to discretize the RANS equations. The computational domain is partitioned into a certain amount of cells and each grid node is surrounded by a control volume. Field information is stored at the center of the cells. Then the cell center values are interpolated into the face values and summed for volume integration. Different interpolation schemes are applied. In detail, a second-order TVD limited linear scheme (Donat and Martinez-Gavara, 2011) is used to discretize the convection terms in Eq. (2); the diffusion term is discretized by a second-order central difference scheme; the Van Leer scheme (Hänel *et al*., 1987) is applied to the VOF equation discretization; a second-order backward method is applied to the temporal discretization. What's more, for the discretized RANS equations, the PISO(pressure-implicit-split-operator) algorithm is adopted to solve the two equations of velocity and pressure. Each PISO loop is made up of three steps, namely prediction, correction and second correction. The second correction can make the velocity and pressure correspond to the momentum equation and continuity equation more effectively.

3 Benchmark computation

The aim of the benchmark computation described in this paper is to validate the reliability of naoe-FOAM-SJTU for the numerical simulations on ship resistance issues. Owing to the many results of the model test, the KCS container ship model without a rudder sailing in calm water is studied for benchmark computation and comparison. The resistance coefficients and flow field were compared with the EFD by Simonsen *et al.* (2013) and Kim *et al.* (2001). The hull geometry of the KCS model is shown in Fig. 1 and the main particulars are listed in Table 1. The scale ratio is 1 : 52.667.

Fig. 1 KCS container ship geometry

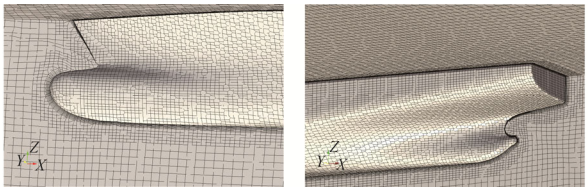

(a) Bow grid (b) Stern grid

Fig. 2 Grids applied in the present work

Table 1 Main particulars of KCS in model scale

Item	Value
L_{pp}/M	4.367
B_{wl}/M	0.611
d/M	0.205
∇/T	0.356
S/m^2	3.436
X_g/M	−0.065
Z_g/M	−0.067

Table 2 Resistance coefficient (F_n=0.26)

Result	Numerical simulation	EFD	Relative error
C_t	4.292×10^{-3}	4.31×10^{-3}	−0.42%

The calm water resistance of the KCS with the Froude number of 0.26 is investigated. The hull is totally fixed without heave and pitch during the simulation. The size of the computational domain is determined as $-1.0\ \mathrm{L} < x < 4.0\ \mathrm{L}$, $0 < y < 1.5\ \mathrm{L}$, $-1.0\ \mathrm{L} < z < 0.5\ \mathrm{L}$. A symmetry boundary condition is used according to the symmetric problem. The size of the grid is nearly 1.09 million and the bow and stern are shown in Fig.2.

The resistance coefficient is defined in Eq. (9).

$$C = \frac{F}{0.5 \cdot \rho S V^2} \tag{9}$$

where C represents the resistance coefficient and F respresents the ship resistance. The results of the present work are listed in Table 2, along with the experimental data from Simonsen. The error rate of the total resistance coefficient is suitably small.

The dimensionless steady wave pattern of the free surface is compared with the EFD in Fig. 3 as well. The contours of the dimensionless wave elevation are displayed. The wave pattern simulated by the naoe-FOAM-SJTU is very close to the measured wave pattern in the calm water experiment. The comparison of the wave profile along the hull surface is also provided for validation in Fig. 4. A good reliability of the present work is shown by the benchmark computation. It is inferred that the naoe-FOAM-SJTU is capable of solving similar problems.

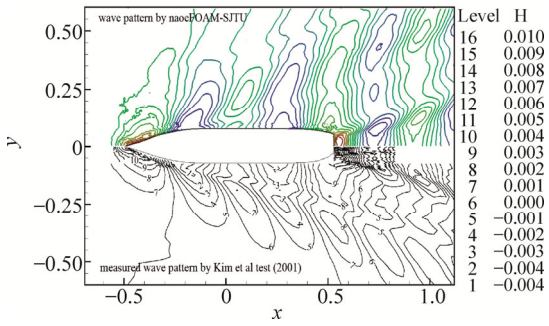

Fig. 3 Wave pattern around the hull (F_n=0.26)

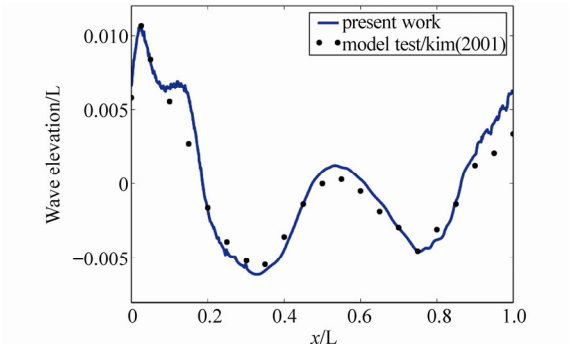

Fig. 4 Wave elevation along hull surface (F_n=0.26)

4 Modeling and mesh generation

4.1 Hull geometries

The numerical simulations of six research vessels are studied in this paper. The main particulars are presented in Table 3 along with the displacement and wetted surface. The features of these hulls are shown in Fig. 5.

Table 3 Main particulars of six hulls (in full scale)

Item	Hull 1	Hull 2	Hull 3	Hull 4	Hull 5	Hull 6
L_{wl}/m	92	90	99	95	88	92
B/m	16.8	17.6	16.0	16.0	17.2	17.0
d/m	5.6	5.7	5.3	5.6	5.8	5.6
C_b/m	0.539	0.532	0.565	0.546	0.545	0.534
∇/t	4773	4918	4840	4760	4940	4789.6
S/m^2	1862.7	1828.4	1810.8	1897.7	1877.5	1852.6

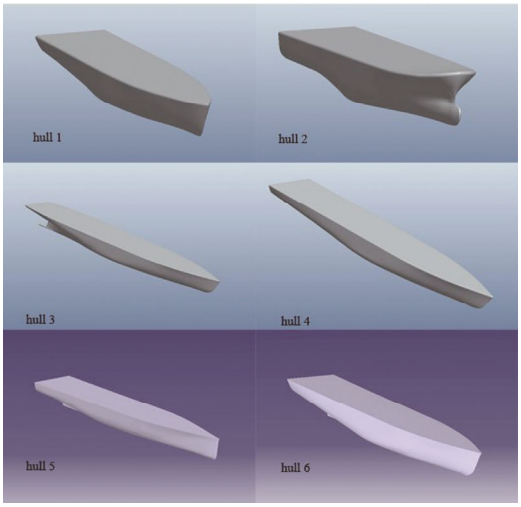

(a) An overall view of six ships

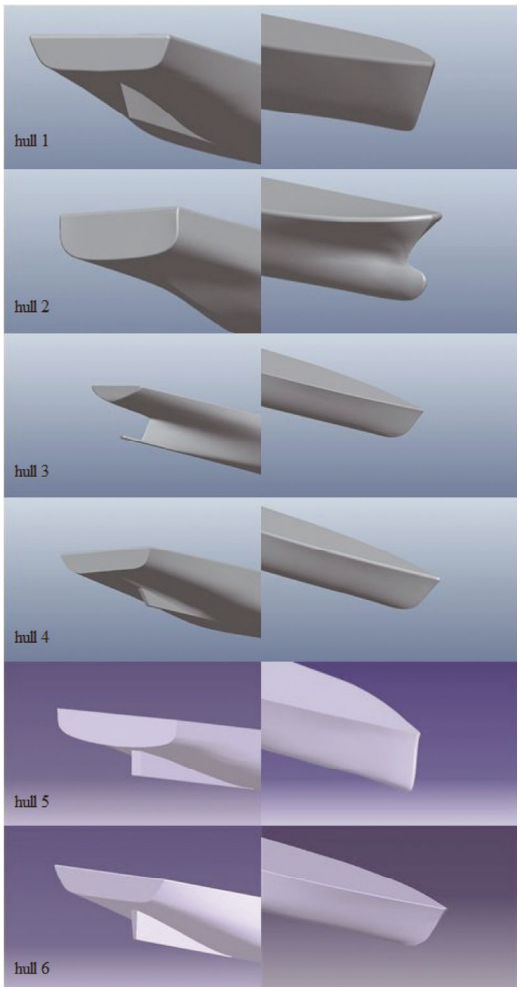

(b) Shapes of the bow and stern of each hull

Fig. 5 Hull geometries

All of these hull forms are designed as research vessels with similar main dimensions in spite of the local differences in the bows and sterns. The raked bows of hulls 1, 3, 4, 6 are similar. Hull 2 has a bulbous bow while hull 5 has an upright stem post at the bow. Hull 3 has a cruiser stern while the transom sterns are adopted for the other five hulls. In terms of the transom stern hulls, except for hull 2, different vertical components are added. The size of the vertical component of hull 4 is smaller than the others. The end of the vertical component of hull 5 is upright while the others are raked. Although their dimensions of different features are not identical, the hull forms of these hulls are similar.

4.2 Computation conditions

According to the practical conditions of commercial ships, the liquid density is 1 024 kg/m^3 based on a sea-water density of 20℃. There are 2 different conditions for each hull, shown in Table 4. The hulls are simulated in a fixed condition without sinkage and trim.

Table 4 Calculation conditions

Hull No.	V/kn	F_n	$R_e/10^8$
Hull 1	12	0.205	5.39
	16	0.274	7.19
Hull 2	12	0.208	5.27
	16	0.277	7.03
Hull 3	12	0.198	5.82
	16	0.264	7.76
Hull 4	12	0.202	5.57
	16	0.270	7.42
Hull 5	12	0.210	5.16
	16	0.280	6.87
Hull 6	12	0.205	5.39
	16	0.274	7.19

4.3 Mesh generation

A same size of the computation domain is applied to these hulls, namely $-1.0\,L < x < 4.0\,L$, $0 < y < 1.5\,L$, $-1.0\,L < z < 0.5\,L$. Because of the symmetrical hull geometry, the practical mesh is generated by a half hull for an optimum computation. *SnappyHexMesh*, the mesh generation utility of OpenFOAM is applied in this paper. The local grid refinements are carried out near the interface and around the hull surface to accurately handle the violent changes of velocity and other variables in the boundary layers. In the present work, the symmetric solution is conducted. A symmetric boundary condition is set for the symmetric problem. The final resistance value of the whole hull is twice that of the resistance calculated by the solver. Without loss of generality, the bow and stern of hull 1 are shown, along with the overall domain mesh in Fig.6.

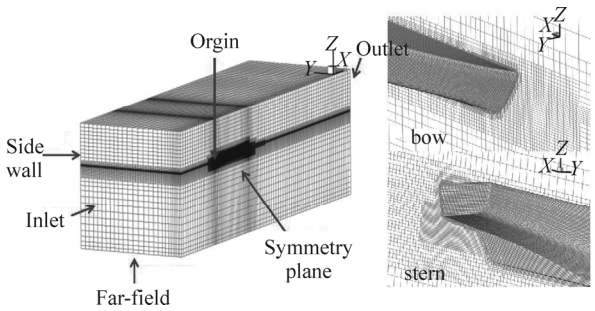

Fig. 6 Mesh generation (hull 1)

5 Analysis of the numerical results

5.1 Mesh convergence study

A study of mesh convergence was conducted for each case. Three types of meshes were generated using the same program respectively and the results are compared.

Hull 1 is taken for an instance to show the results of the mesh convergence study. The iteration results and the errors between the results of the adjacent grid size cases are shown in Table 5. C_p represents the pressure resistance coefficient; C_v represents the friction resistance coefficient; C_t represents the total resistance coefficient, equaling to the

sum of C_p and C_v. As the coefficients against the mesh number at 12 kn and 16 kn show in Table 5, the convergence of the resistance computation is achieved.

Table 5 Mesh convergence study of hull 1

V/kn	Grid size/10^6	C_p/ 10^{-3}	C_v/ 10^{-3}	C_t/ 10^{-3}	R_t/N	Error/%
	0.73	2.54	1.69	4.23	1.54	—
12	0.96	2.31	1.83	4.14	1.51	1.95
	1.64	2.21	1.85	4.06	1.49	1.32
	0.73	4.04	1.70	5.74	3.71	—
16	0.96	3.81	1.78	5.59	3.61	2.70
	1.64	3.77	1.76	5.53	3.57	1.11

Table 6 Precision limits computation

V/kn	R_{t1}/N	R_{t2}/N	R_{t3}/N	$\overline{R}$/N	P_r
12	1.54	1.51	1.49	1.513 3	0.020 548
16	3.71	3.61	3.57	3.630 0	0.058 878

The uncertainty assessments need to be studied for verification and validation. According to the ITTC Quality Manual (1999), benchmark computations are useful in development and confirmation of verification procedures in code development. For the CFD uncertainty analysis, the numerical errors and uncertainties mainly result from the iterative solution methods and various input parameters such as spatial and time step sizes. The errors and uncertainties are highly dependent on a mass of specific application (geometry and conditions). The total uncertainty contains the bias and precision limits. For simplification, the precision limits of the total resistance from these three grids are calculated by Eqs. (10) and (11). The grid arrangement possesses an expected practicability and adaptability for different conditions. The results of the finest mesh computations are analyzed.

$$P_r = 2 \cdot \sqrt{\frac{\sum_{k=1}^{N}(R_k - \overline{R})^2}{N(N-1)}} \tag{10}$$

$$\overline{R} = \frac{1}{N} \cdot \sum_{k=1}^{N} R_k \tag{11}$$

5.2 Results analysis

The drag coefficient components of all hulls at 12 kn and 16 kn are shown in Fig.7 and Fig. 8, respectively. The friction resistance coefficients calculated by the ITTC-1957 formula are also presented for comparison. Obviously the total resistance coefficients at 16 kn are higher than those at 12 kn. Both at 12 kn and 16 kn, the total resistance coefficient of hull 3 is the smallest while that of hull 5 is the largest. For the other four hulls, the performances are similar at 12 kn. However, at 16 kn, the total resistance coefficient of hull 1 increases apparently beyond those of the other four hulls.

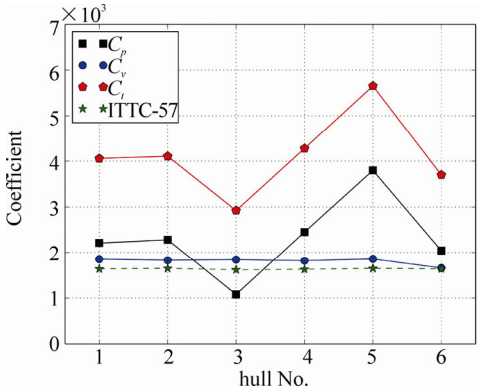

Fig. 7 Drag coefficients of different hulls at 12 kn

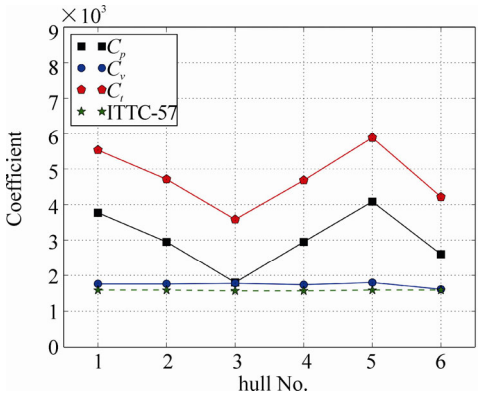

Fig. 8 Drag coefficients of different hulls at 16 kn

Each hull has an approximately equal friction resistance coefficient but a remarkably different pressure resistance coefficient. For a specified hull, the friction drag coefficient decreases slightly with the increase of velocity. An increase of the Reynolds number leads to a reduction of the thickness of the boundary layer, which results in a decline of the plumpness of the flow velocity distribution within the boundary layer. As a result, the value of the friction shearing stress τ will increase with the Reynolds number. However, the increase rate is less than the square of the hull velocity. As a result the friction drag coefficient still decreases with the increase of the Reynolds number. Generally the values change a little from 12 kn to 16 kn. For different hulls at the same speed, according to the hypothesis of the equivalent plank, the similar friction resistance coefficients are obtained by a tiny difference of wetted surface. The variation of the total resistance is mainly related to the pressure resistance, including the viscous pressure resistance and wave resistance.

In Fig. 7 and Fig. 8, it is shown that the increase rate of the pressure drag coefficient of hull 1 is the greatest, which reaches almost 70.6%. Second is hull 3, which reaches almost 66.7%. The pressure drag coefficient of the other four hulls grows a little. In particular, with the maximum drag coefficient, the resistance increase rate of hull 5 is the minimum, which is only 7.4%.

5.3 Wave profiles

The wave resistance can be qualitatively investigated by the wave height distributions along the hull surface. By

capturing the free surface contour line, the wave elevations can be obtained. The non-dimensional wave profiles of all the hulls at both 12 kn and 16 kn are shown in Fig. 9.

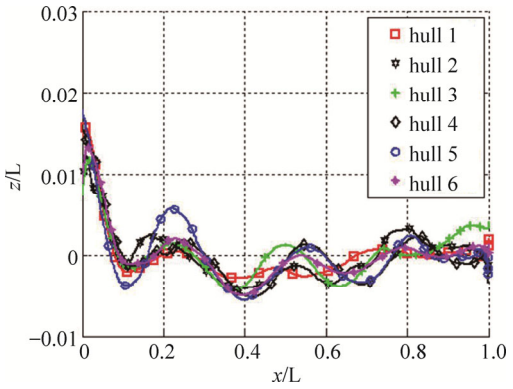

(a) 12 kn

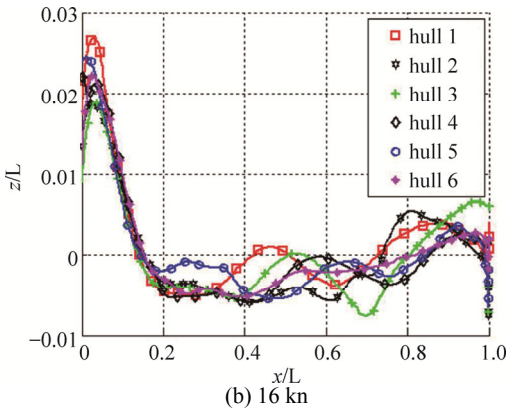

(b) 16 kn

Fig. 9 Wave elevations of different hulls

At 12 kn, the wave elevation in the fore region of hull 5 is the highest. The curves of the other five hulls have a similar trend. The location and amplitude of the wave crest and trough are nearly the same. At 16 kn, the main crests are observed near the bow and aft hull, which is different from the 12 kn cases. The wave elevations of hull 1 and hull 5 are higher than those of the other four hulls. The wave-making energy is provided by the hull, which is proportional to the square of the wave height. In terms of hull 5, a wave with a higher crest results in more energy consumption of the hull, so a bigger wave resistance is obtained. The wave resistance of hull 1 becomes larger than that of the others, second only to that of hull 5. The curves of hull 3 at 16 kn are much heavier than at 12 kn, which leads to the high increase rate of the pressure drag coefficient.

5.4 Free surface

Wave making is a significant factor for the ship's resistance. The wave patterns are captured when the steady flow field is formed. For instance, the free surfaces at 16 kn are shown in Fig. 10. The situations at 12 kn are analogous.

The steady wave-making can be investigated, especially near the bow. The wave making near the hull conforms to the results of the wave profile in Fig. 9. The wave patterns after the stern region can be studied in Fig. 10. At the same velocity, the wave making of hull 5 is larger than hull 1. However, with the velocity increasing, especially at a high Froude number, the difference is significantly reduced. The bulbous bow of hull 2 is one of the important factors in restraining the wave amplitude at high speed. Furthermore, from Fig. 10, the freeboard of hull 5 or hull 1 is smaller than that of hull 2. As the models are fully fixed, the resistance component by sinkage and trim is neglected. And the small freeboard may result in green water at high velocity, which would worsen the resistance performances.

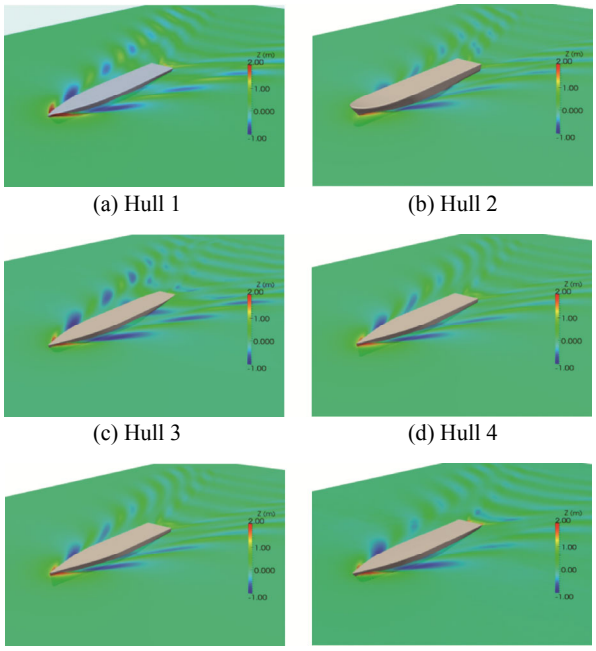

(a) Hull 1 (b) Hull 2

(c) Hull 3 (d) Hull 4

(e) Hull 5 (f) Hull 6

Fig. 10 Comparison of the free surface and wave pattern of different hulls at 16 kn

5.5 Dynamic pressure distribution around the hull

The pressure difference is a significant element for resistance analysis of different hulls. The location and value of the pressure peak at the bow and stern regions of the four typical hulls at 16 kn are shown in Fig. 11. At higher velocity, more discernible effects of the different hull forms on the pressure distributions are inferred.

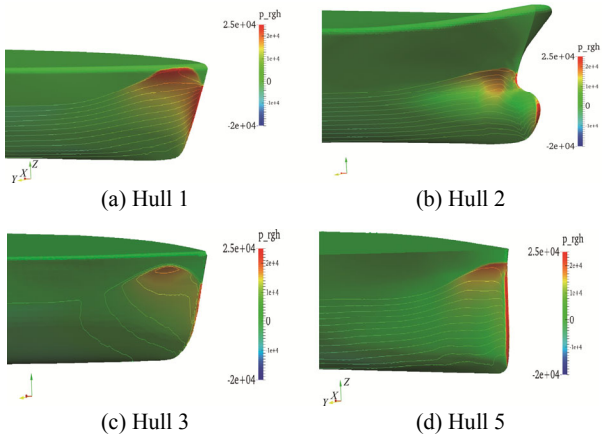

(a) Hull 1 (b) Hull 2

(c) Hull 3 (d) Hull 5

Fig. 11 Pressure at the bow of hulls 1, 2, 3, 5 at 16 kn

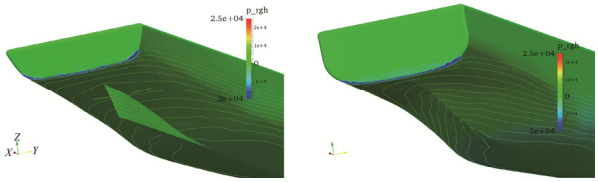

(a) Hull 1 (b) Hull 2

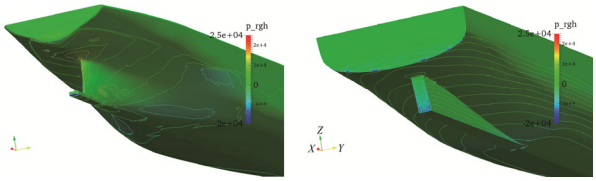

(c) Hull 3 (d) Hull 5

Fig. 12 Pressure at the stern of hulls 1, 2, 3, 5 at 16 kn

As shown in Fig. 11 and Fig. 12, the region of the peak pressure of hull 1 is apparently larger than that of the other hulls, which mainly covers the wave crest near the bow. The region of the peak value of hull 2 is mainly at the intersection of the stem post and designed waterline, and at the most forward part of the bulbous bow. Away from the regions above, the pressure would decrease rapidly. Especially for the bulbous bow of hull 2, a lower pressure exits except for at the front location. The pressure distribution of hull 4 or hull 6 is identical to that of hull 3. The region of the peak pressure is concentrated on the stem post instead of the crest near the bow. From the waterline to the bottom of the hull on the stem post, the value of the pressure decreases gradually. The value of the peak pressure is more uniform for the stem post of hull 5. In addition, the pressure on the crest near the bow of hull 5 is greater than that of hull 3. For the pressure at the stern, an obvious stripe of low pressure locates on the bottom of the stern transom plate. The pressure distribution of hull 3 is more irregular than hulls 1, 2 and 5. In sum, the larger pressure gradient around the surface is one of the reasons why the viscous pressure resistance of hull 5 is greater than that of the other hulls.

5.6 Streamlines near the hull

The streamlines near the bows of the two typical hulls at 16 kn are shown in Fig. 13. The streamlines of the other hulls are similar to hull 1. The streamlines near the stern also affect the hydrodynamic performance asdisplayed in Fig. 14. In Fig. 13, all of the hulls except hull 2 have a similar bow streamline distribution. The overall streamline mode is smooth and laminar. The velocity magnitude near the bow crest is lower than the other regions. The results are in accordance with the analysis of the free surface and pressure distribution. As shown in Fig. 14, after the stern transom plate of hull 2 or hull 5 the streamlines are more turbulent. Many intensive eddies are generated so that the pressure at the stern is reduced. The large pressure difference between the field of the hull's bow and stern leads to an increase in the viscous pressure drag. In particular, eddies also exit after the vertical component at the stern of hull 5, giving rise to a high viscous pressure drag. It can be inferred that the end face of the vertical component seems too steep, or the vertical component is too thick in the *Y*-axis direction. On the contrary, the vertical component at the stern of hull 3 or hull 4 is useful to rectify and smooth the streamlines, while hull 2 has no vertical component. Hull 1 and hull 6 produce some slight turbulent streamlines after the stern, so their performances are not as good as hull 3 or hull 4.

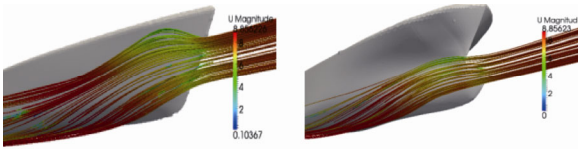

(a) Hull 1 (b) Hull 2

Fig. 13 Streamlines near the bows of hull 1 and hull 2

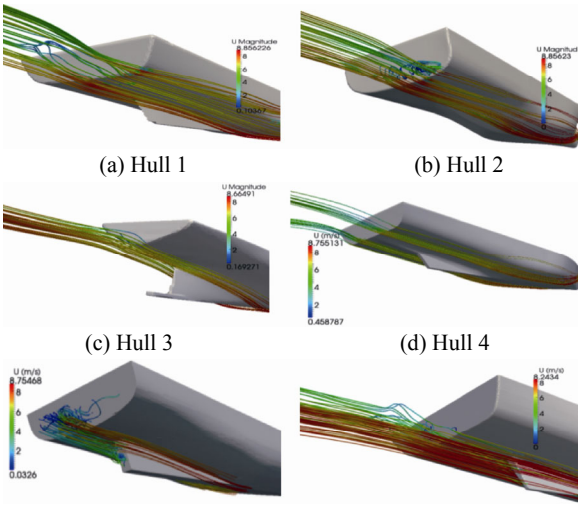

(a) Hull 1 (b) Hull 2

(c) Hull 3 (d) Hull 4

(e) Hull 5 (f) Hull 6

Fig. 14 Streamlines near the stern of all the hulls

5.7 Vorticity field

The generation of vortices would cause a severe pressure reduction and vibration of the hull. Thus studying the vortices around the hull is very useful to evaluate the resistance performance for the hull form design.

The vortices distribution near the hull at 16 kn is more distinctive for comparison. By slicing 18 transverse sections on the hull along the *X*-axis, the vortices can be effectively presented as seen in Fig. 15.

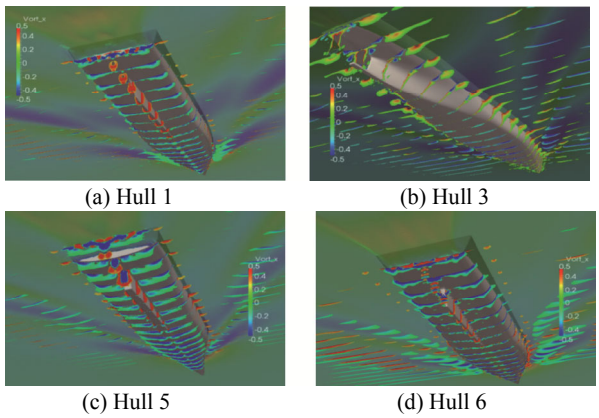

(a) Hull 1 (b) Hull 3

(c) Hull 5 (d) Hull 6

Fig. 15 Vorticity field of hulls 1, 3, 5, 6 at 16 kn

The status of hull 2 and hull 4 is similar to hull 6. For these four hulls, large amounts of irregular eddies are generated near the vertical component at the stern, and the bottom of the hull before the center of hull 5 and hull 1. The region of high magnitude of the vorticity of hull 1 or hull 5 is larger than that of the other hulls. For hull 5 at high velocity, the vortices region is smaller while the amplitude of the vortices is larger. By contrast, less eddies are observed not only on the free surface but also on the bottom of the hull of hull 3 and hull 6. Meanwhile the region of the peak value of the vortices is small and sporadic. On the free surface of hull 3 and hull 6, some miniature vortices are generated as well. The vortices on the bottom of the hull lead to the formation of low pressure. For hull 5 and hull 1, due to the large region and high intensity of the vortices, the viscous pressure is accreted. It can be inferred that the performance of hull 1 is worse when sailing at high speed. The appearance of the bow trim in practical situations will also exacerbate the increase of resistances.

5.8 Wake field at the field

A homogeneous wake field is significant for resistance and the propulsive performance of a ship. In this paper, the cross section of x/L=0.9 at earth's coordinate is chosen to show the wake field. The wake shape of each hull will not be identical if the velocity changes, but the difference can be neglected. Therefore, only the wake field at 12 kn is shown in Fig. 16. The contours indicate the distribution of the dimensionless velocity component in X direction while the curves represent the streamlines in the Y-Z plane.

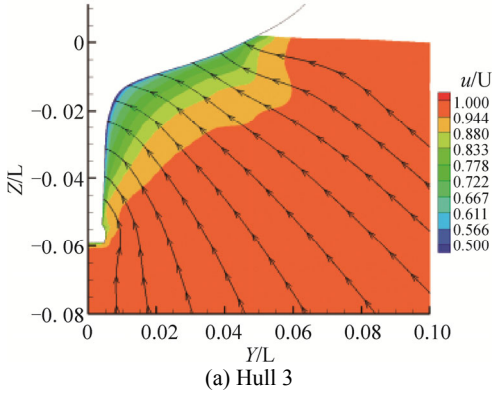

(a) Hull 3

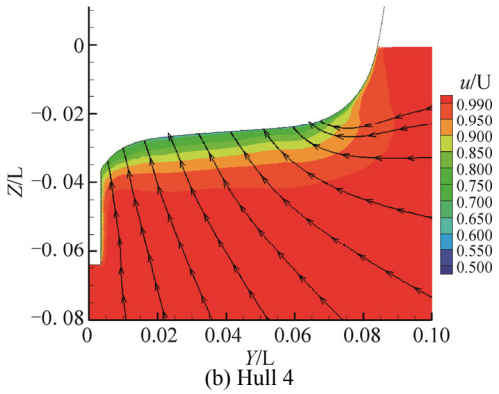

(b) Hull 4

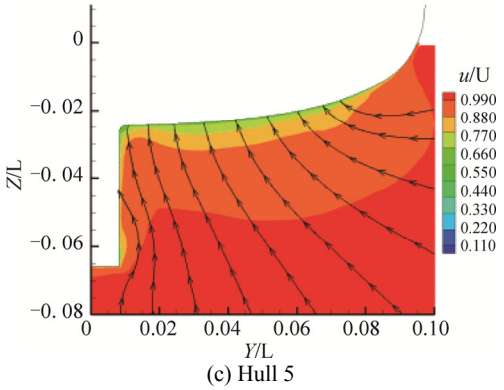

(c) Hull 5

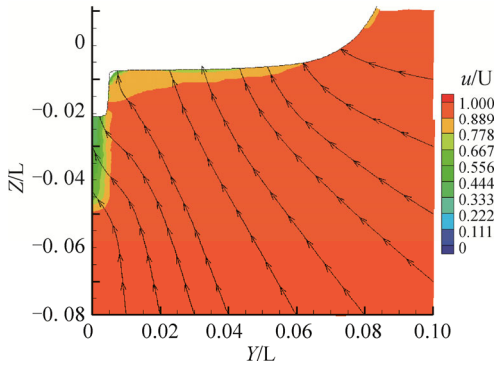

(d) Hull 6

Fig. 16 Wake field at the stern of hulls 3,4,5,6 at 12 kn

In Fig. 16, hull 5 has an inhomogeneous wake compared to the other hulls. For hull 4, the wake region does not cover the surface of the vertical component, which means the vertical component has little influence on the flow field. Although the wake field of hull 6 is larger than that of hull 5, the homogeneity of hull 6 is better. It can be inferred that the propulsive performance of hull 5 is unsatisfactory while the feature of hull 3 or hull 6 is recommended.

6 Conclusions

In this paper, the resistance performances of six similar hulls are studied by using the solver naoe-FOAM-SJTU. According to the results of the ship resistances in calm water, at either 12 kn or 16 kn, the resistance performance of hull 3 is the best while hull 5 performs the worst among the six hulls. The other four hulls have their different features. Hull 1 is appropriate when sailing at low velocity, because the resistances increase heavily when the speed grows higher. The advantage of hull 2 lies in the bulbous bow and the large freeboard. A good seakeeping performance of hull 2 can be inferred. Among them, hull 4 has a mediocre resistance performance. For hull 6, the vertical component avoids the mass of eddies, indicating a low pressure resistance.The propulsive performance of hull 6 is desired due to the homogeneous wake field.

It is necessary to consider the different aspects for hull 5 to improve the resistance performance. It is the higher viscous pressure resistance that leads to the worse

performance of hull 5 at 12 kn (F_n=0.2), instead of the wave resistance. However, 16 kn is within the range of high speed (F_n=0.28). The proportion of the friction drag is decreased while the wave drag plays a more important role in the total resistance. The stern form and vertical component of hull 5 should be improved in accordance with that of hull 3 or hull 6, which can reduce the vortices and vicous pressure resistances at low velocity. The bulbous bow of hull 2 may improve the wave-making resistance performance at high velocity. However further studies need to be performed to determine the location and size of the bulbous bow. The raked bow of hull 6 brings a relatively slender water plane above the load water plane and a larger area of the deck, which can also be adopted by hull 5 to reduce the wave-making resistance at high speed. Through these approaches, a better resistance performance of hull 5 can be obtained. The conclusions based on the simulation results will provide good references for the design and construction of research ships.

Nomenclatures

α	Relative proportion of the two phase fluid
B_{wl}	Breadth of waterline
C_b	Block coefficient
C_p	Pressure drag coefficient
C_v	Friction drag coefficient
C_t	Total drag coefficient
d	Draft
F_n	Froude number
L_{pp}	Hull length between perpendiculars
L_{wl}	Hull length of waterline
ρ	Fluid density
p_d	Dynamic pressure
P_r	Precision limit
R_e	Reynolds number
R_t	Total resistance
S	Wetted surface
U	Velocity field
V	Ship speed
X_g	Longitudinal center of gravity
Z_g	Vertical center of gravity
$\triangle$	Displacement

References

Bal S (2008). Prediction of wave pattern and wave resistance of surface piercing bodies by a boundary element method. *International Journal for Numerical Methods in Fluids*, **56**(3), 305-329.

Barton IE (1998). Comparison of SIMPLE and PISO type algorithms for transient flows. *International Journal for Numerical Methods in Fluids*, **26**(4), 459-483.

Cao HJ, Wan DC (2012). Numerical investigation of extreme wave effects on cylindrical offshore structures. *Proceedings of the Twenty-second International Offshore and Polar Engineering Conference*, Rhodes, Greece, 804-811.

Cha JJ, Wan DC (2011). Numerical wave generation and absorption based on OpenFOAM. *China Ocean Engineering*, **29**(3), 1-12.

Dawson CW (1977). A practical computer method for solving ship-wave problems. *Proceedings of the Second International Conference on Numerical Ship Hydrodynamics*, Berkeley, USA, 30-38.

Donat R, Martinez-Gavara A (2011). Hybrid second order schemes for scalar balance laws. *Journal of Scientific Computing*, **48**(1-3), 52-69.

Hänel D, Schwane R, Seider G (1987). On the accuracy of upwind schemes for the solution of the Navier-Stokes equations. AIAA, Honolulu, USA, Paper 87-1104.

Hino T, Martinelli L, Jameson A (1993). A finite-volume method with unstructured grid for free surface flow simulations. *Proceedings of the 6th International Symposium on Numerical Ship Hydrodynamics*, Iowa City, USA, 173-193.

ITTC Quality Manual (1999). *Uncertainty analysis in CFD uncertainty assessment methodology*. The 22nd ITTC, Seoul and Shanghai, Report No. 4.9-04-01-02

Jasak H, Jemcov A, Tukovic Z (2007). OpenFOAM: A C++ library for complex physics simulations. *International Workshop on Coupled Methods in Numerical Dynamics*, Dubrovnik, Croatia, 1-20.

Kim WJ, Van SH, Kim DH (2001). Measurement of flows around modern commercial ship models. *Experiments in Fluids*, **31**(5), 567-578.

Shen ZR, Jiang L, MIAO S, Wan DC (2011). RANS simulations of benchmark ships based on open source code. *Proceedings of the Seventh International Workshop on Ship Hydrodynamics*, Shanghai, China, 76-82.

Shen ZR, Cao HJ, Wan DC (2012). *Manual of CFD solver for Ship and Ocean Engineering Flows*: *naoe-FOAM-SJTU*. Shanghai Jiao Tong University, Shanghai, China, Technical Report No. 2012SR118110.

Shen ZR, Wan DC (2013). RANS computations of added resistance and motions of a ship in head waves. *International Journal of Offshore and Polar Engineering*, **23**(4), 263-271.

Simonsen CD, Otzen JF, Joncquez S (2013). EFD and CFD for KCS heaving and pitching in regular head waves. *Journal of Marine Science and Technology*, **18**(4), 435-459.

Weymouth GD, Wilson RV, Stern F (2005). Rans computational fluid dynamics predictions of pitch and heave ship motions in head seas. *Journal of Ship Research*, **49**(2), 80-97.

Ye HX, Shen ZR, Wan DC (2012). Numerical prediction of added resistance and vertical ship motions in regular head waves. *Journal of Marine Science and Application*, **11**(4), 410-416.

Author's biography

Decheng Wan is a professor of CFD for Marine hydrodynamics at the School of Naval Architecture, Ocean and Civil Engineering, Shanghai Jiao Tong University, and a distinguished professor of Shanghai Eastern Scholar. His research interests include marine hydrodynamics and computational fluid dynamics, marine numerical wave tanks, nonlinear wave theory, fluid-structure interaction, vortex-induced vibration for risers, offshore renewable energy, high performance computation for complex flows, *etc.*